3D Printing of Liquid Crystal Polymers for Space Applications

Houriet, C.C.M.C.A.G.; Claassen, Evelien ; Mascolo, Chiara; Jöhri, Haimo ; Brieva, Abel ; Szmolka, Szilvia ; Vincent-Bonnieu, Sebastien; Suliga, Agnieszka ; Masania, Kunal; More Authors

DOI
10.1002/admt.202400571

Publication date
2024

Document Version
Final published version

Published in
Advanced Materials Technologies

ADVANCED MATERIALS TECHNOLOGIES
www.advmattechnol.de

3D Printing of Liquid Crystal Polymers for Space Applications

*Caroline Houriet, Evelien Claassen, Chiara Mascolo, Haimo Jöhri, Abel Brieva, Szilvia Szmolka, Sébastien Vincent-Bonnieu, Agnieszka Suliga, Raphael Heeb, Silvan Gantenbein, Ugo Lafont, Thomas Rohr, and Kunal Masania**

Fused Filament Fabrication is a promising manufacturing technology for the circularity of space missions. Potential scenarios include in-orbit applications to maximize mission life and to support long-term exploration missions with in situ manufacturing and recycling. However, its adoption is restricted by the availability of engineering polymers displaying mechanical performance combined with resistance to space conditions. Here, a thermotropic Liquid Crystal Polymer (LCP) is reported as a candidate material with extrusion 3D printing. To expand its scope of applicability to structural parts for space applications, four different exposure conditions are studied: thermal cycling under vacuum, atomic oxygen, UV, and electron irradiations. While 1 MeV-electron irradiation leads to a green coloration due to annealable color centers, the mechanical performance is only slightly decreased in dynamic mode. It is also found that increased printing temperature improves transverse strength and resistance to thermal cycling with the trade-off of tensile stiffness and strength. Samples exposed to thermal cycling and the highest irradiation dose at lower printing temperatures still display a Young's modulus of 30 GPa and 503 MPa of tensile strength which is exceptionally high for a 3D-printed polymer. For the types of exposure studied, overall, the results indicate that LCP 3D-printed parts are well suited for space applications.

1. Introduction

The European Space Agency (ESA) aims to implement a circular economy in space by 2050.[1] While in the 20th century, space was strictly limited to a very small number of governmental actors, in the 21st century, a "New Space" economy is developing. It is characterized by a diverse collection of actors such as private enterprises, startups, and universities.[2] The global reduction in satellite size has also coincided with a sevenfold increase in the number of satellites orbiting Earth in 10 years, with constellations of small satellites now representing their majority. Within the same time frame, the number of CubeSats has also been multiplied by 25.[3] In this context, to avoid the piling up of space debris, mitigate the threat they pose on operational satellites, and make the industry sustainable, new aspects start to be considered in mission designs. In-orbit servicing, in-orbit assembly, in-orbit manufacturing, and eventually in-orbit recycling projects are envisioned in future developments.[4] Given its extensive design freedom, strong automation capabilities, and versatility in raw material selection, additive manufacturing (AM) is a key technology to facilitate Out-of-Earth manufacturing, compared to traditional manufacturing methods for satellite structures, such as composite layup or machining of metal alloys.[5] Fused Filament Fabrication (FFF) works well in microgravity due to its reliance on a pressure difference to extrude, as demonstrated by 3D printers already functional on the ISS, as well as the MELT 3D printer[6] and the

C. Houriet, E. Claassen, K. Masania
Shaping Matter Lab
Faculty of Aerospace Engineering
Delft University of Technology
Kluyverweg 1, Delft 2629 HS, Netherlands
E-mail: k.masania@tudelft.nl

The ORCID identification number(s) for the author(s) of this article can be found under https://doi.org/10.1002/admt.202400571

DOI: 10.1002/admt.202400571

C. Mascolo, R. Heeb, S. Gantenbein
NematX AG
Förrlibuckstrasse 150, Zürich 8005, Switzerland

H. Jöhri
Paul Scherrer Institute
Forschungsstrasse 111, Villigen 5232, Switzerland

A. Brieva, S. Szmolka, S. Vincent-Bonnieu, A. Suliga, U. Lafont, T. Rohr
ESTEC, European Space Research and Technology Centre
Keplerlaan 1, Noordwijk 2201 AZ, Netherlands

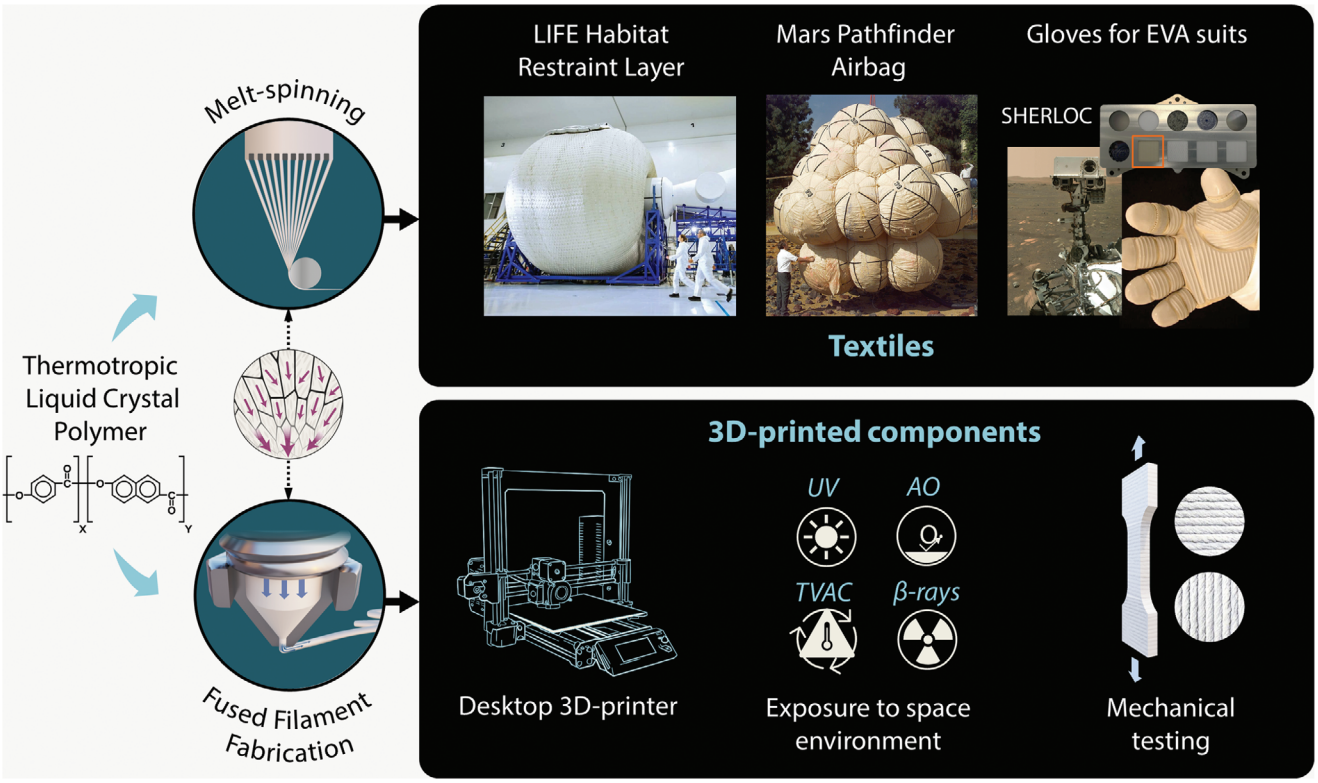

Figure 1. Overview of the Vectra 3D-printing process as opposed to melt-spinning of Vectran. During melt-spinning, alignment is obtained via elongational flow. During 3D printing, the nematic domains in the liquid crystal state also align as they undergo elongational flow, as well as shear flow inside the nozzle. To evaluate the space-worthiness of the 3D-printed polymers, it is exposed to four different components of the space environment; UV-irradiation, atomic oxygen, thermal cycling, and high-energy electron irradiations (known as beta-rays). Subsequently, it is evaluated for its optical, chemical, and mechanical changes. Image credits: NASA, Sierra Space.

IMPERIAL 3D printer[7,8] developed in collaboration with ESA. FFF has also the advantages of high customizability of components and high shaping freedom. However, the use of FFF for space applications has been restricted by the moderate mechanical properties of available materials compared to traditional ones, such as aluminum, titanium or composite structures, especially when it comes to withstanding the extensive loads during launch.[5,9] Within the selection of polymers that are suitable for the extreme space environment, few have demonstrated compatibility with FFF such as PEEK,[10,11] or PEI.[12–14] In particular, the MakerSat-1 CubeSat, deployed in orbit in 2020, was the first satellite to use a fully 3D-printed frame. It embedded material durability experiments on 3D-printed polymers. After 4 months of exposure, the PEI/PC (Ultem) blend showed a 20.9% mass loss, which was attributed to space environmental degradation and especially to the effect of atomic oxygen erosion.[14]

The emergence of thermotropic liquid crystal polymers as printable material could prove to be disruptive for space applications. Indeed, the thermotropic liquid crystal polymer HBA:HNA with a ratio 73:27 has been used under a fiber form in the space environment, often referred to by its commercial tradename Vectran. Being non-polar and with an aromatic backbone, it possesses high thermal and chemical resistance properties combined with high mechanical performance.[15–17]

As a fabric, its good fold characteristics have resulted in its use for safety and protection such as for parachutes and the Pathfinder airbags.[18] It is also one of the structural components of the restraint layer of the Bigelow Expandable Activity Module currently deployed on the ISS.[19] More recently, it has been selected for the LIFE habitat of Sierra Space for its mechanical performance for the same purpose. A full-size test unit of 300 m^3 using Vectran fibers woven into straps, or webbings, was recently tested to failure, exceeding NASA safety levels by 27%.[20] Furthermore, it has been used as a highly cut-resistant material for the palms and fingers of astronaut gloves during EVAs.[21,22] Its properties are currently further investigated in situ on Mars with the SHERLOC module, integrated into the Perseverance rover.[23] SHERLOC is capable of periodically analyzing the composition of Martian rocks and four fabrics considered for future space suits, including Vectran. The results of their exposure to the Martian atmosphere, radiations, dust, and thermal cycling will guide the design of future Mars-specific spacesuits.[23] Overall its usefulness as a space material under its melt-spun form is undoubtedly present and has attracted great interest as shown in **Figure 1**.

Recently, FFF was employed to process this polymer, instead of melt-spinning.[24–27] A parallel can be drawn between the contraction die geometry inside the 3D-printer nozzle, and the spinneret during the melt-spinning process which both enable the alignment of the nematic domains during extrusion, granting the polymer its remarkably high mechanical properties compared to injection-molding. Due to the large temperature difference between the nozzle (T = 295 °C or higher) and the ambient

environment, the polymer is solidified before full relaxation of the nematic domains can take place, leading to a strong molecular anisotropy in the printing direction.[24]

In contrast to other approaches where anisotropy is obtained by the top-down combination of a matrix and a fiber, this method utilizes the bottom-up capability of rigid-rod polymer chains to self-align along a favored orientation of shear and elongational flow. Similarly, while natural materials, such as wood, bone, or nacre, are made of weak building blocks, the strength and toughness they possess are granted by their hierarchical arrangement and anisotropy.[28] In LCP, this molecular anisotropy is controllable with printed line width, leading to tailorable stiffness and strength on the fly.[26] Spatial gradients of mechanical behavior can be embedded within one part, between high-stiffness (30 GPa) associated to low-strain regions, and lower stiffness (3 GPa) with large-deformation regions. Furthermore, lines can also be spun by the 3D printer itself, akin to the melt-spinning manufacturing of Vectran fibers, thus creating reinforcement and matrix made of the same material.[25] To our knowledge, such a palette of deposition methods and available mechanical properties with one single material and a desktop printer is unprecedented.

The 3D printing of LCP therefore indicates a complementary scope of uses to the traditional melt-spinning method, for various structural and functional objects. For instance, the highly packed chains in the nematic state also grant the material a low free volume, giving rise to good gas-barrier properties as well as mechanical strength. As such, its low permeability[27] may prove useful for applications in liquid or gas retention in space. An extensive material selection survey was performed by Slejko et al.[9] across 3D-printable polymers and metals, considering structural requirements like specific stiffness (using injection-moulding values for polymers) and heat for demise during atmospheric re-entry for debris mitigation purposes. This survey indicated that LCP was the only polymer approaching the performance of the best metal choices according to this metric. In the context of out-of-Earth manufacturing and future permanent human settlement on the Moon or Mars, the potential capability of this polymer to be reprocessed after its first life as Vectran fabric, and especially reused as FFF-feedstock should be further noted.

However, while the polymer backbone is the same between 3D-printed LCP (3DP-LCP) and melt-spun LCP (MS-LCP), the strong influence of processing parameters and methods on most material properties is a well-known feature of this kind of thermotropic LCPs.[29–31] FFF is also known to create inhomogeneities inside the part, such as voids.[32,33] These may pose a concern as LEO (Low Earth Orbit) and GEO (Geostationary Earth Orbit) orbits expose the spacecraft to a harsh environment consisting of atomic oxygen (for LEO), solar UV photons, heavy ions, solar flare protons, as well as protons and electrons trapped in belts by the Earth's magnetic field.[34] The exact application of such a material for space hardware does also depend on its durability in the respective space environment. Therefore, there is a need to assess the space-relevant characteristics of 3DP-LCP to evaluate its potential as a structural bus for CubeSats, or other applications in orbit and on planetary settlements.

To establish whether 3DP-LCP possesses similar resistance to the space environment to MS-LCP, four different types of exposure were selected: thermal vacuum cycling (TVAC), Vacuum UV, high energy electron irradiation, and lastly exposure to atomic oxygen (AO) via the Euro Material Ageing campaign carried out by ESA and CNES.[35] Further characteristics studied here are outgassing and change in thermo-optical properties after exposure. Mechanical response is measured after thermal vacuum cycling, for two different printing configurations, four printing temperatures, and with the highest dose of electron irradiation. Dynamical Mechanical Analysis (DMA) and Fourier-Transform Infrared Spectroscopy (FTIR) were also used to gain insight into potential polymer degradation. The polymer performance is compared to data available for MS-LCP and 3D-printable candidates such as PEEK and PEI. We show that 3DP-LCP retains its pre-exposure mechanical properties, despite some drastic appearance changes under UV and electron irradiation.

2. Results and Discussion

2.1. Exposure of 3DP-LCP to Simulated Space Environment

2.1.1. Vacuum

Quantifying the magnitude of outgassing is crucial to assess the space-worthiness of polymers, to avoid contamination of optics and other critical surfaces by the volatile organic compounds (VOC) released under exposure to vacuum at elevated temperatures.[36,37] These chemicals, which are impurities, space environmental degradation products, or left-over from chemical reaction or cleaning steps, migrate and escape via diffusion and desorption, respectively.[36] Potential contaminants may increase the outgassing phenomenon in the 3D-printed LCP compared to the melt-spun form Vectran because the polymer is extruded twice after being received in the form of pellets: First to be spooled as a 3D-printing filament and second through the nozzle of a 3D printer during manufacturing.

Figure 2 shows the outgassing performance of 3DP-LCP compared to literature values for Vectran[38] and PEEK.[11] In Figure 2a, results for total mass loss after exposure to vacuum are almost identical for Vectran and 3DP-LCP. Residual mass loss (RML) is the mass loss after water reabsorption during post-conditioning, thus it represents the total mass loss of the specimen without the absorbed water. The lower RML for 3DP-LCP indicates that it is more prone to absorbing moisture than the Vectran rope. For both metrics, the 3DP-LCP shows less outgassing than 3DP-PEEK. However, in all cases, values are below 1% RML, the maximum threshold according to ECSS standards.[39] The testing apparatus, a Micro Volatile Condensable Measurement facility could not collect any CVCM (Collectible Volatile Condensable Material). A Residual Gas analysis was therefore carried out on 3DP-LCP to analyze released gases in high vacuum. Figure 2b shows the chemical composition of outgassed compounds for two types of samples exposed to vacuum during 48 h: with and without 24 h of prior bake-out at 150 °C. A small amount of hydrocarbon can be observed on the pristine sample, but not when bake-out has occurred. Figure 2c indicates that after bake-out, the outgassing rate has reached a level close to the high vacuum limit (1.0×10^{-10} mbar L s^{-1} cm^{-2}). The sample without bake-out shows an outgassing rate two orders of magnitude lower than 3D-printed PEEK.

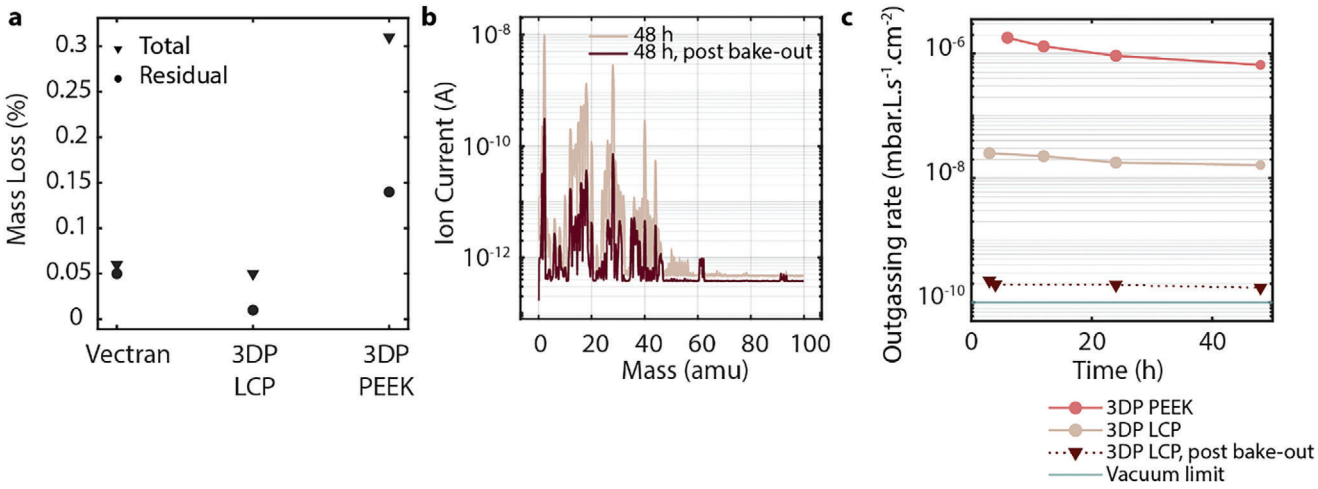

Figure 2. Pristine 3D-printed LCP (3DP-LCP) outgassing properties compared to another polymer (PEEK) and Melt-Spun LCP (MS-LCP), also known as Vectran. A) Total Mass Loss and Residual Mass Loss indicate lower values for the Vectran fiber rope[38] and 3DP-LCP than for 3DP-PEEK.[11] In all cases, values are acceptable per ECSS-Q-ST-70-02C.[39] A residual gas analysis enables to obtain. B) indications of the molecular composition of the outgassed compounds and, C) outgassing rate over time, showing two orders of magnitude decrease in outgassing rate when the polymer has been baked out for 24 h at 150 °C.

Meeting outgassing requirements is a necessary condition for space applications, which both melt-spun and 3D-printed LCP fulfill. However, contamination can still arise from the reaction of the material through space environmental exposure. For example, in LEO, Atomic Oxygen (AO) can be damaging to the external materials of a spacecraft.[34] The oxygen atom, which is a result of the photodissociation of dioxygen with UV irradiation, has one unpaired valence electron and is therefore highly reactive. With the orbital velocity of a spacecraft, the energy of an atomic oxygen impacting the surface is ≈4.5 eV, sufficiently high to break chemical bonds. It is however not reaching a sputter threshold of ≈30 eV, and thus materials degradation follows an oxidative erosion mechanism.[40] Therefore, exposed organic surfaces in particular tend to erode gradually. On top of the gradual reduction in thickness, low mass volatile reaction by-products can be emitted, increasing the risk of further contamination of critical surfaces.

2.1.2. Atomic Oxygen

In LEO, such as the altitude of ISS (400 km), AO constitutes one of the most important contributors to material degradation, as it tends to impact the surface of exposed structures.[34] Moreover, it is the most abundant species found between altitudes of 180 to 650 km. During a pre-flight qualification step of the Euro Material Ageing study organized by ESA, 3DP-LCP was exposed to 2.0×10^{21} atoms cm^{-2} in a space environment simulation facility, under high vacuum and 15–40 °C temperature range. AO damage can often be seen with a change in the color or dullness of the material. In **Figure 3a**, the 3D-printed samples were compared to reference and did not sustain visible changes. Solar absorptance and thermal emittance were measured as they help determine the thermo-optical characteristics of the spacecraft. Solar absorptance increased slightly from 0.27 ± 0.03 to 0.32 ± 0.03 after exposure. The thermal emittance coefficient increased from 0.87 ± 0.05 to 0.93 ± 0.05. This change in properties is usually linked to the erosion and formation of roughness of the surface of the samples due to AO.[34] To assess the extent of damage, the specimens are observed in SEM and compared to pristine counterparts in Figure 3b. The microstructure of 3DP-LCP exposed to AO is typical for organic materials with a carpet-like microstructure caused by oxygen etching away and then penetrating inside the formed holes.[47] Vectran fibers of a fabric exposed to AO with a fluence of 2.2×10^{20} atoms cm^{-2} at 200 °C also show this microstructure.[41]

The erosion damage of 3DP-LCP can be quantified by measuring the erosion yield, which is the volume of material removed per incident impacting atom. It is compared in Figure 3c against high-performance 3D-printable thermoplastics (PEEK and PEI) and MS-LCPs under different forms. All data except that of the fabric[41] and the 3D-printed samples come from flight missions such as NASA MISSE-7 where specimens are attached to ISS (ram or wake) and brought back to Earth for analysis. The erosion yield of the 3DP-LCP is $2.18E^{-24}$ cm^3 $atom^{-1}$. In a previous study, 3D-printed conductive PEEK was also measured with $1.98E^{-24}$ cm^3 $atom^{-1}$.[11] This is in a typical range of thermoplastic polymers. The expected thickness loss of the 3DP-LCP is estimated to be 0.1 mm per year in the context of the Euro Material Ageing study where samples will be exposed to a LEO environment within the Bartolomeo module of the International Space Station. In real use for long-term missions in low orbits, protective coatings are being used.[34] For instance, a Vectran mesh coated with polyurethane[45] was shown to limit AO damage by an order of magnitude.

In Figure 3d, an Ashby chart compares erosion yield to specific stiffness, that is, the ratio of Young's modulus to density, for typical 3D-printable polymers, as well as Vectran, epoxy resins, and polyimide. 3DP-LCP has the advantage of a very high specific stiffness that can be tailored via the width of the printed lines as shown in.[26] This possibility is illustrated by the large span in specific stiffness on the graph. The interaction of AO with metals is different: Non-volatile metal oxides are typically produced as a

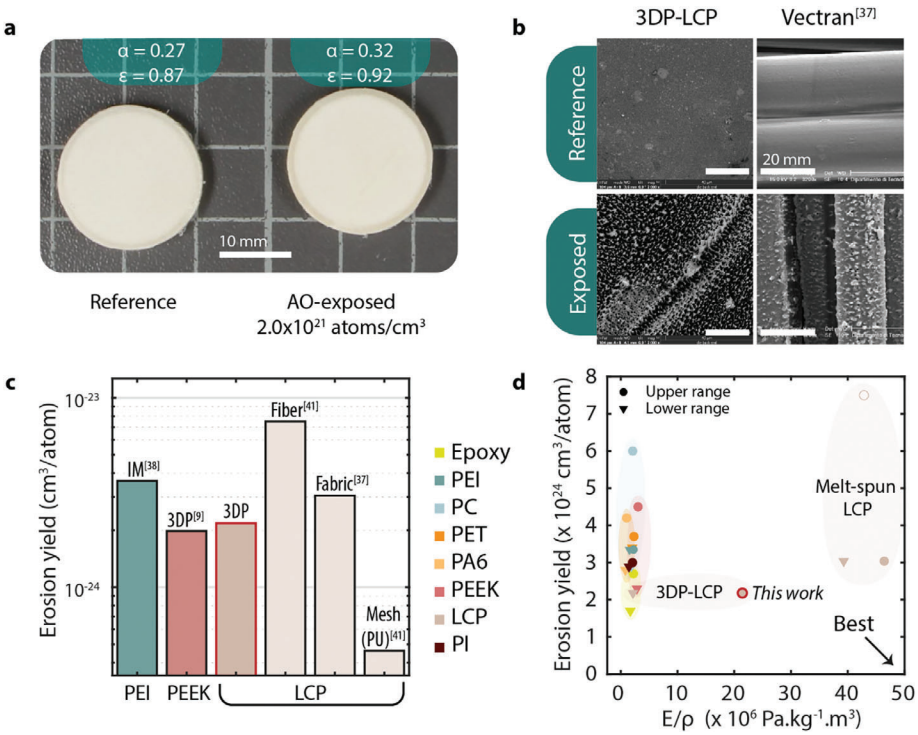

Figure 3. Exposure of 3DP-LCP to Atomic Oxygen (AO). A) No visible change can be spotted after exposure. B) Surface damage becomes noticeable in SEM micrographs, with a typical "carpet-like" pitted pattern. This behavior is comparable to that of MS-LCP with Vectran fibers.[41] C) Erosion yield is compared to 3DP-LCP and MS-LCP under different forms. 3DP-LCP behaves in the range of other 3D-printable polymers, such as 3DP-PEEK[11] and PEI.[42] On a flown Vectran mesh (Mission MISSE-7,[43]) a polyurethane coating imparts further resistance to AO. D) An Ashby diagram compares erosion yield to specific tensile stiffness for different polymers, including 3D-printable ones. Polymers: PEI – polyetherimide (ULTEM), PC – polycarbonate, PET – polyethylene terephthalate (Mylar), PA6 – Polyamide-6 (Nylon), PEEK – polyether ether ketone (Victrex), LCP – liquid crystal polymer (Vectran), PI – polyimide (Kapton). The dot circled in red corresponds to the average specific tensile stiffness obtained for 3DP-LCP between printing temperatures of 295 and 310 °C. Erosion yield is extracted from NASA-flown missions,[44,45] stiffness-density ranges from Ansys Granta Selector database[46] and from.[12,26]

result of their oxidation. These oxides tend in most cases to shield the surface below and reduce any further damage. Therefore the metric of erosion yield is not meaningful and they do not appear on this graph. While erosion resistance is a great advantage for metals, as pointed out in[9], LCPs with the addition of protective coatings should still be considered when metrics such as shaping freedom are valued in the case of a CubeSat structure.

One can notice a large variation in erosion yield in MS-LCP. The highest erosion yield has been reported at 7.5×10^{-24} cm^3 atom^{-1} for a yarn,[48] while in MISSE-2[45] a Vectran fabric displays an erosion yield of 1.08×10^{-25} cm^3 atom^{-1}. This order of magnitude difference was attributed in[45] to the presence of an oil-based T150 weaving finish, absent in the non-woven yarns. Moreover, other factors may play an important role as well. Variability in erosion yields during different MISSE missions has been related to the variation in solar exposure. AO has a synergetic effect with UVs, which can cause the photoaging of polymers.[49]

2.1.3. UV-Irradiation

Spacecraft outside of Earth's atmosphere are subjected to the full solar spectrum of the Sun. Relevant wavelengths are the VUV (Vacuum UV) and Near UV (NUV) spectra, between 100 and 400 nm. UV-irradiation is known to be extremely damaging to most polymers, as it is energetic enough to cause the breakage of organic bonds, such as C=C, C=O, or C—H.[50]

Vectran fibers in particular contain ester groups, which are known to undergo photochemical reactions, leading to chain scission and thus decrease in mechanical properties. A tenfold decrease in mean strength is for instance reported between no exposure and 336 h of exposure under a Xenon lamp by Liu et al.[51] Such exposure also typically shows a transition from a smooth, defect-free structure, to the occurrence of roughness, delamination, and fissures. The degree of fiber structure ordering is also decreased. The mechanism of photoaging has been studied for Vectran in the N_2 environment[51] and involves the scission of the C—O bond within the ester group (C=O—O).

In **Figure 4**, a 3DP-LCP sample was exposed to VUV/UV conditions with an acceleration factor of 6.7 suns in a high vacuum environment for 432 h between 65 and 100 °C. This amounts to ≈2900 solar hours. The UV damage can be assessed visually in Figure 4a thanks to the shadowing effect of the sample holder shown in Figure 4b. Significant yellowing can be noticed with exposure. This results in a significant increase in the solar

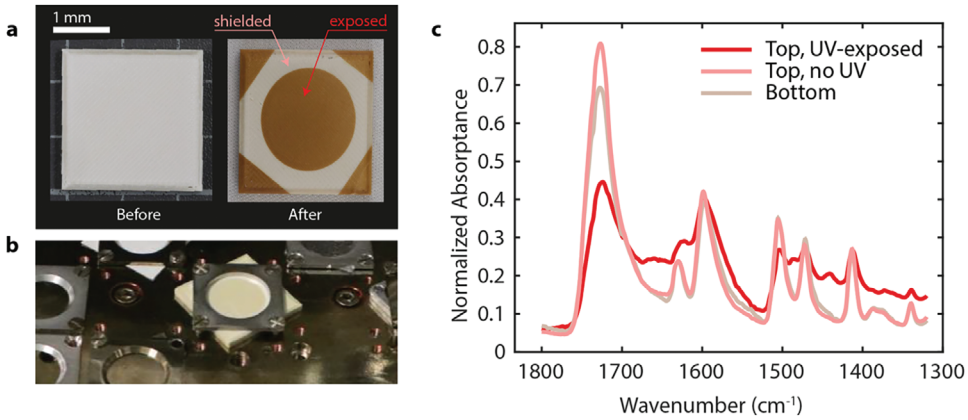

Figure 4. Exposure of 3DP-LCP to VUV/UV irradiation. A) The specimen shows significant discoloration in the exposed locations which can be compared to the ones shielded by B) the sample holder. C) Fourier-Transform Infrared Spectroscopy (FTIR) is performed to evaluate changes in the chemical nature of the surface. The top surface is evaluated at two different points (central zone exposed in red, and edge zone sheltered in pink) and compared to the center of the bottom surface (beige).

absorptance from 0.27 to 0.52. However, thermal emittance stayed constant at 0.87. Further investigation was conducted with Fourier-transform Infrared Spectroscopy (FTIR) in Figure 4c to understand the chemical nature of the damage. Spectra at three locations were obtained: First, two un-exposed locations at the top and the bottom of the part. Bottom refers to the side in contact with the bed during printing, and to the cold plate during exposure. Another location corresponds to the center of the top surface, with UV damage. The spectra were normalized by their highest peak at a higher wavenumber. The intensity of the 1600 cm^{-1} peak is almost identical between all measurement locations, which can be attributed to the aromatic ring stretching of HBA.[51] The most prominent peak for the unexposed location is associated with the carbonyl group (C═O) stretching out-of-plane at 1727 cm^{-1}. Its drop in intensity from 0.80 to 0.40 between the two upper locations may indicate that the ester group has been undergoing a photochemical reaction as suggested in.[51] At the UV-exposed location, a peak at 1440 cm^{-1} is present, contrary to the unexposed locations. This peak can be attributed to the O—H bending of the carboxylic acid. This may indicate breakage of the polymer chains and a higher number of terminations of the chains or radicals. These elements indicate that chain scission also occurs in photo-aged 3DP-LCP, like many aromatic copolyesters.[15]

In essence, while the chemical consequences of photoaging between 3DP-LCP and MS-LCP for UV resistance are similar, the difference lies more in their respective scale of use: the diameter of Vectran fibers is ≈20 µm.[15] In contrast, a 3D-printed functional piece displays a layer height of 100 µm and is composed of dozens to hundreds of layers, leading to a typical size in the order of centimeters. ≈95% of incident radiation below 250 nm is absorbed within a depth of 0.3 µm for most polymers.[52] Therefore, the bulk of the 3D-printed components is not exposed, as shown in the cross-section of the exposed sample in Figure S1 (Supporting Information). Furthermore, in light of the low penetration depth of the UV photons, coatings are also effective in shielding the polymer. For example, titanium dioxide coatings have been studied specifically to reduce superficial UV damage in Vectran fibers.[53,54]

Both UV and ATOX are related to superficial damage. However, other types of radiation can penetrate much deeper into materials because of their higher energy, such as protons, electrons, heavier ions, and energetic photons such as X-rays and gamma rays.[34] These fall under the category of ionizing radiation, as they can ionize atoms as they move through matter. Degradation caused by radiations in polymers is based on the same mechanisms that those occurring during UV exposure, linked to either chain scission or cross-linking depending on the type of polymer.[55]

2.1.4. Beta Irradiation

Several types of charged particle radiations occur in space: galactic cosmic rays, solar proton events, and trapped particles in radiation belts. In LEO below the radiation belts, damage from particle radiations may be overshadowed by degradation caused by UV and AO for the duration of a mission. Particle radiation damage becomes important to consider in GEO and deep space mission environments. Solar Particle Events strong enough to endanger astronaut health are rare, on the occurrence of one per decade.[56] Nevertheless, long transit times involved with deep-space missions call for a better understanding of these phenomena on materials. Furthermore, the solar wind can penetrate the Martian atmosphere, giving rise to dose rates of low-energy protons and electrons similar to those encountered inside the ISS.[57] Depending on mission type, cumulated doses on optical elements have been estimated to range between 1 krad and 500 krad when non-directly exposed to the space environment, and 1 Mrad to 180 Mrad, respectively for LEO and GEO, when exposed.[58]

The penetration depth of a particle increases with its energy.[59] To maximize possible damage within the bulk of the material, LCP samples are irradiated with high-energy electrons (1 MeV) in a Van de Graaf accelerator shown in **Figure 5a**. Even though the synergetic effect of different radiation types (protons, heavy ions, electrons) cannot be reproduced, cumulated doses are chosen to compare to those of LEO and GEO missions. Three different doses are selected: 10^{14}, 10^{15}, and 10^{16} e^{-} cm^{-2}. This is

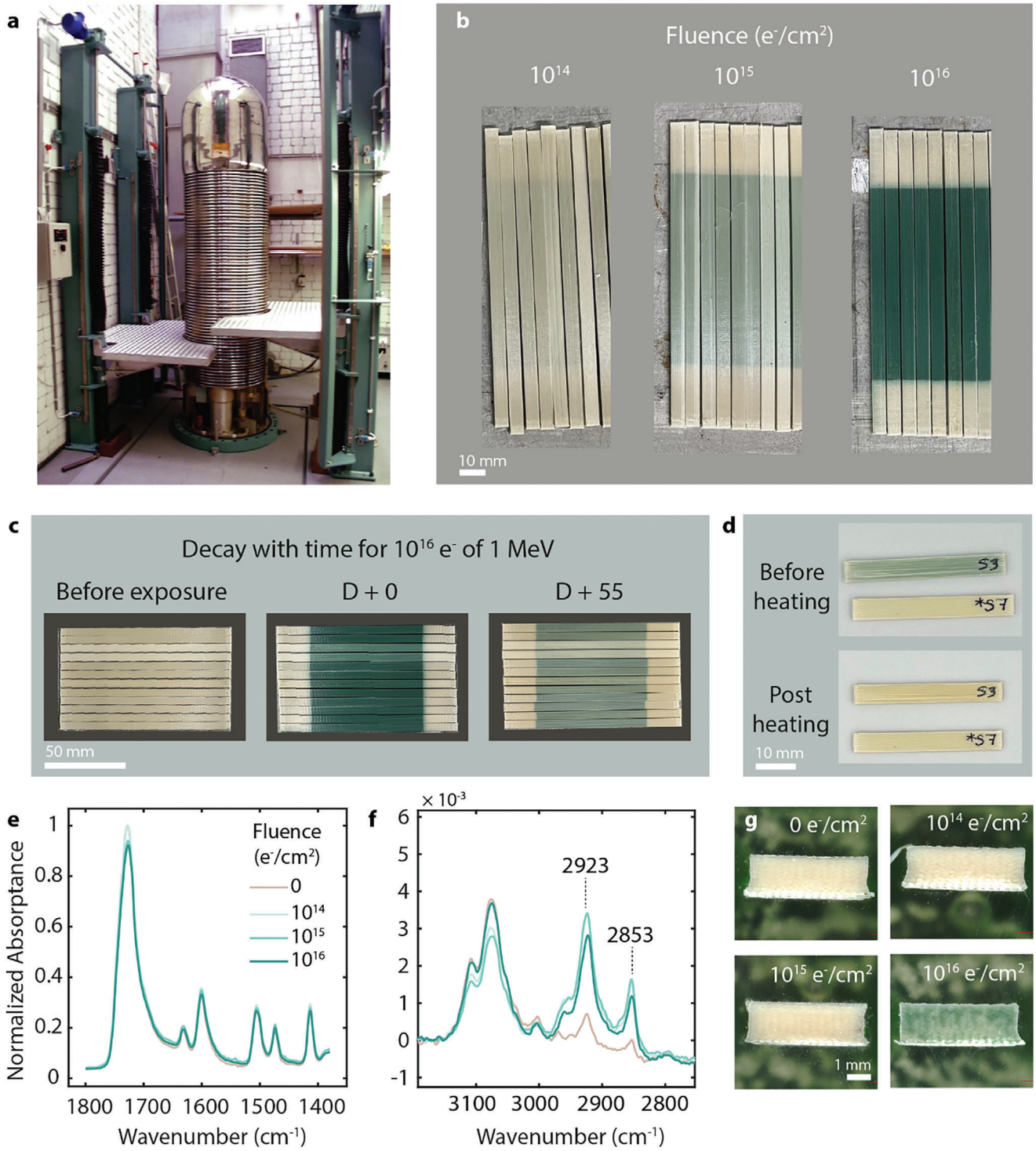

Figure 5. Exposure of 3DP-LCP to beta irradiations. A) A Van der Graaf accelerator is used to send 1 MeV electrons onto 3D-printed specimens. B) Three different fluences are applied (10^{14}, 10^{15}, and 10^{16} e^- cm^{-2}), resulting in an important change in coloration from almost none to a vibrant green. C) This color change can be attributed to trapped electrons inside the polymer matrix (color centers). The specimen coloration fades away with time, and stabilizes between 20 to 55 days. D) The non-permanent nature of the color center is evidenced by annealing samples for 1 h under 200 °C. While the pristine specimen (bottom) does not display any visible color change, the specimen with the highest fluence has lost its coloration. E) FTIR spectra do not show any significant difference between pristine samples and the three irradiation doses at low frequencies. F) However, a difference is noticed at ≈ 2923 and 2853 cm^{-1}. These absorption peaks are typically attributed to the stretching of the C-H bonds. G) Micrographs of cross-sections indicate that the color centers are present uniformly throughout the depth of the highest-dose sample. In contrast, color centers cannot be seen for the lower fluences six months after irradiation.

equivalent to accumulated doses of 2.92, 29.2, and 292 Mrad, assuming linearity as detailed in Table S1 (Supporting Information). Three different batches of tensile samples are exposed corresponding to these different doses. Figure 5b shows photographs obtained directly after exposure. Sample color can be compared between sample extremities, which are unexposed thanks to lead shields, and center. A change to dark green can be noticed, with intensity increasing with the fluence.

The origin of the color change is attributed to so-called color centers, first observed in single crystals in the late 19th century.[60] For polymers, the work of Wallace and Clough et al.[61,62] have led to the classification of radiation-induced color centers between two types: annealable and permanent. Annealable color centers have been associated with free radicals trapped within rigid polymer matrices, such as cyclohexadienyl or benzyl.[62] The annihilation of free radicals happens via diffusion of O_2 (oxygen quenching), or the combination of one color center with another (self-quenching). The process is typically accelerated by heating above the glass transition, which facilitates molecular motion.[63]

Color centers caused by irradiations have already been reported for many optical polymers,[61,64] polycarbonate,[65] and polystyrene,[66] which tend to turn from transparent to shades of yellow or dark brown with gamma irradiations. Some epoxy glasses were also reported to display a greenish color after electron irradiation.[67,68] However, to our knowledge this is the first time that a liquid crystal polymer, or a 3D-printed polymer, is reported to display color centers.

The intensity of the color with the largest fluence fades away rapidly before stabilizing after 20 days, as shown in Figure S2 (Supporting Information). Furthermore, the hue completely disappears with exposure to 200 °C for 1 h, as shown in Figure 5d. These elements suggest that the color centers created by the electron beam are of the annealing kind. A relationship between the increasing proportion of annealable centers and lower permeability has been previously noted,[63] which is in line with the low gas permeability of the LCP studied here.[27] The temporal and reversible nature of this color change indicates that the polymer network has not been dramatically changed by radiation. This is also supported by the FTIR spectra of pristine samples compared to radiated specimens of 3 different doses in Figure 5e. In contrast to the UV-exposed specimen in Figure 4c, the spectra are rather similar. A difference can however be noted between the pristine sample and irradiated ones in Figure 5f, where the relative amplitude of two absorption peaks at 2923 and 2853 cm^{-1} is increasing. These absorption peaks are typically attributed to C—H bond stretching.[69] In the work of Hou et al.[68] an epoxy was exposed to 170 keV electrons at the same fluence range as this work. A similar green coloration was observed after irradiations. This was associated with a decrease in the 2923 cm^{-1} peak with increasing fluence. In this case, the diamino- diphenylmethane (DDM) structure present in this epoxy, containing a methylene group linking two phenyl groups which was shown to transform into a quinone-type radical upon irradiation. It is hypothesized that a similar mechanism should occur within this polymer, with further study needed to identify its precise origin.

Unlike previous exposure types, the relatively high energy of the irradiated electrons was chosen to enable the 2 mm-thick specimens to be affected throughout their depth. The experimental relative dose versus penetration depth in water of 1 MeV with the Van der Graaf accelerator used in this study is shown in Figure S3 (Supporting Information). The dose is at its maximum (147% of surface dose) at a depth of 1.8 mm. While the media is different, the order of magnitude of penetration in the polymer is similar. Cross-sections of samples with the three increasing fluences are shown in Figure 5g, compared to a non-exposed specimen, 6 months after exposure. For samples with fluences of 10^{14} and 10^{15} e^- cm^{-2}, no visible difference to the pristine sample can be noticed. In contrast, the specimen with 10^{16} e^- cm^{-2} fluence is still marked after six months with a green shade throughout its depth. The uniform presence of color centers indicates that the irradiations have penetrated the bulk of the polymer. Any alteration to the polymeric network should therefore have consequences on the mechanical properties of these specimens, which are discussed next.

2.2. Mechanical Properties of Exposed Materials

2.2.1. Influence of Radiation and Thermal Cycling on Mechanical Properties

Dawes et al.[55] report that the dominant effect of high-energy irradiation on polyesters is chain scission, although both chain scission and cross-linking can occur. Since the LCP studied here is of the class polyester-arylate, one should investigate which of the two occurs. The important change in appearance and the indication of methylene group appearing with irradiation in FTIR spectroscopy indicate that some damage may be expected at these doses.

To study the impact of electron irradiation on mechanical properties, two types of specimen are therefore studied, respectively for tensile test under quasi-static load and flexural bending under dynamical load using DMA. In both cases, the direction of printing (0°) is aligned with the longitudinal dimension. Some of the specimens with the largest irradiation dose are also subjected to TVAC (thermal vacuum cycling for 25 cycles between −100 and +100 °C), and their properties are compared to non-cycled counterparts. Indeed, a synergetic effect of thermal cycling and irradiation occurs in the space environment.[70] When irradiated and unirradiated composites were thermally cycled between −157 and +121 °C, higher microcrack density and mechanical property change were found for the irradiated composites.

The Young's modulus and ultimate tensile strength (UTS) are plotted in **Figure 6a** for tensile specimens exposed to different conditions. Several observations can be made: first, despite the strong difference in coloration and differences noticed in FTIR in Figure 5f, the three different fluences, 10^{14}, 10^{15}, and 10^{16} e^- cm^{-2}, do not show any difference in stiffness or UTS. Second, the impact of TVAC on the irradiated sample cannot be seen. The samples exposed with the highest dose, which belong to the same printing batch, behave the same whether they have been exposed to 25 thermal cycles in vacuum or not. Furthermore, the samples that are tested as closest to exposure to the space environment (TVAC'd and radiated with the highest dose estimated at 292 Mrad) still show an average Young's modulus of 29.8 ± 3.8 GPa and 525 ± 30.1 MPa of UTS. As shown in Figure S5 (Supporting Information), the samples fail in a catastrophic fashion typical of composites with strong anisotropy. The fibers revealed

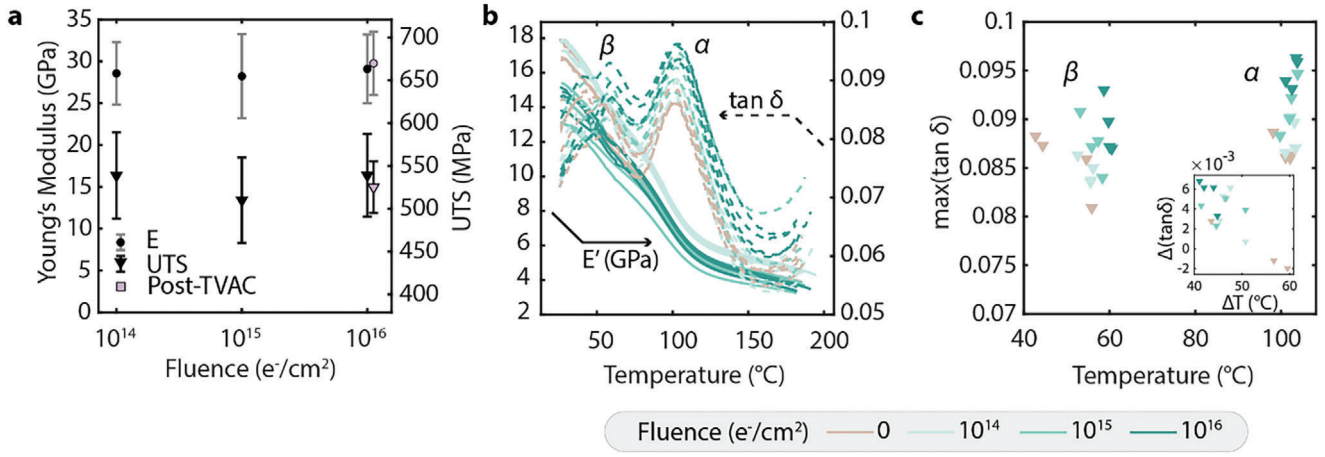

Figure 6. Impact of electron irradiation on quasi-static and dynamic mechanical properties. A) Young's modulus and Ultimate Tensile Strength (UTS) of exposed samples do not show a significant difference with increasing fluence, even after Thermal Vacuum Cycling (TVAC). Error bars represent standard deviation. B) Three-point bending dynamical mechanical Analysis at 10 Hz and 0.1% strain indicate a gradual softening in the storage modulus with increased irradiation dose. C) This softening is further noticed in the evolution of the damping factor tan δ. The first relaxation increases in magnitude and temperature with increasing dose, while the second relaxation only increases in magnitude. The insert indicates the difference in amplitude and temperature between the α- and β-peaks.

from the inside of the fractured sample also show a characteristic green color due to penetration of the β-radiations.

Dynamical Mechanical Analysis (DMA) allows a finer description of the sample behavior with temperature and usually indicates molecular changes in the material. Figure 6b shows the effect of temperature on storage modulus and damping factor tan δ for the three irradiation doses. Two relaxations are noticed, as previously reported in.[29,71,72] The lowest relaxation, termed β, taking place at ≈60 °C, corresponds to the motion of the hydroxynaphthalene (HNA) moiety. The other relaxation, named α, is associated with cooperative motions of both HNA and HBA, akin to a glass transition, taking place close to 100 °C. Typically before any exposure, the β-relaxation is more intense than the α-relaxation. This is reported to change after 5 h of annealing.[29] In our case, the α-relaxation is higher even for the pristine sample. One should however note that what we considered "pristine" has already been processed twice: first into a filament and second to be 3D-printed.

Across the temperature range, two distinct groups are noticed. The storage modulus of pristine and 10^{14} e^- cm^{-2} specimens is higher than that of the specimen with higher doses (10^{15} and 10^{16} e^- cm^{-2}). This is also noticed in Figure 6c, where the amplitudes of the relaxation peaks are plotted against the temperature at which they occur. The insert shows the corresponding difference in amplitude and temperature between α- and β-peaks. Both low-irradiation and the pristine specimens display similar magnitude for their α-and β-peaks. For the most irradiated specimen, the α-peak has a higher magnitude than the β-peak (positive value). Interestingly, the temperature of the β-peak increases with fluence, but the values for higher fluence are closer to those of literature (≈60 °C). The fact that storage modulus is lower throughout the range for the specimen irradiated with 10^{15} and 10^{16} e^- cm^{-2}, supports the hypothesis of degradation of the samples with high exposure rate, and possible chain modification, as suggested in Figure 5f. However, the plausible degradation at this high dose does not enable us to notice statistically significant changes in unidirectional tensile performance in quasi-static testing at room temperature.

2.2.2. Influence of Printing Temperature

In the space environment, temperatures can vary rapidly from either extreme, for instance −160 °C in the Earth's shadow and 120 °C in direct sunlight in low earth orbit.[73] Extremes can even coexist within the same exposed piece. This thermal cycling present throughout the mission life can be an important contributor to material damage. Thermal expansion can cause critical thermal stresses leading to thermal fatigue.[74]

In the case of LCP, the coefficient of thermal expansion (CTE) depends on processing conditions and the state of anisotropy of the material. MS-LCP displays an axial CTE of −5.78 µm/(m·K).[75] This can be explained by the fact that when the stiff chain vibrates as temperature rises, its projection becomes shorter along the longitudinal axis.[76] The CTE of 3DP-LCP in the X-direction is also slightly negative (−2.4 µm/(m·K)), as shown in Figure S4 (Supporting Information). The anisotropy of the 3D-printed object makes the value differ from injection-molded or melt-spun LCP, especially in the Z-direction, with a value of 198 µm/(m·K). The particularly high anisotropy of CTE has been observed before in 3D-printed carbon-fiber polycarbonate, for which a CTE of 210 µm/(m·K) was reported.[77] Graphite is another example of a layered material where the layered direction is much weaker than the planar one.[78,79] Such a discrepancy compared to the X-axis is linked to the fact that the chains tend to vibrate along the direction where interchain interactions are weaker.[76]

Since high discrepancies in expansion upon heating are observed depending on the printing direction, thermal cycling may also be more harmful to the polymer in the interlaminar direction. To test this hypothesis, two types of specimens were manufactured. Unidirectional samples, with the printing direction

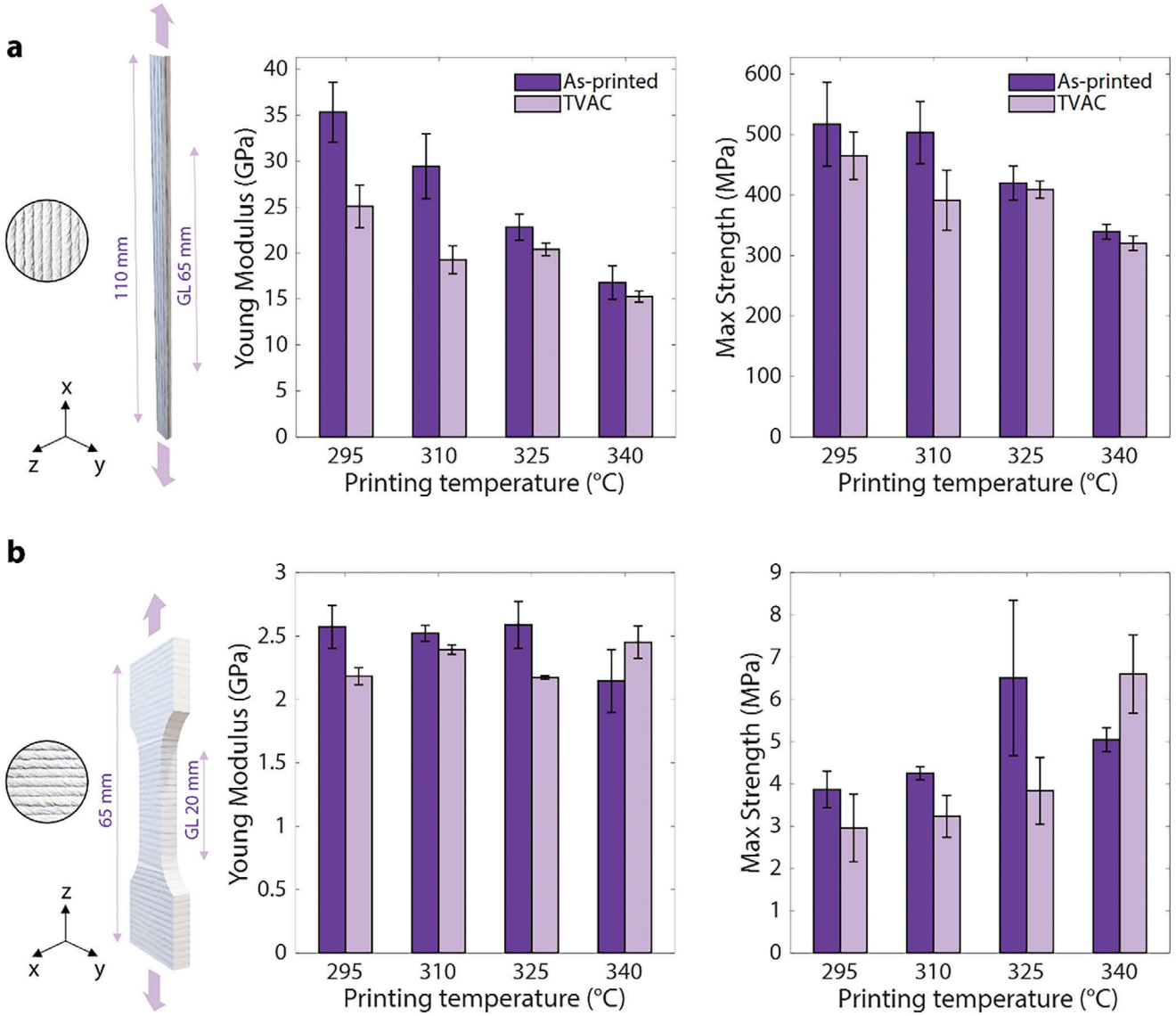

Figure 7. Mechanical testing of samples tested in A) longitudinal direction, coinciding with the printing direction, and B) normal to the printing plane. Two different batches are compared, with and without exposure to TVAC, for different printing temperatures, illustrating the strong influence of processing conditions. The printing direction is represented in inserts with the unit vector Z. The specimen geometry is shown with its longitudinal dimension and gauge length (GL). Error bars represent standard deviation.

aligned with the loading direction, are shown in **Figure** 7a. Dog-bone-shaped samples with the loading direction aligned with the Z-direction are shown in Figure 7b. A batch was printed and tested directly while another batch was first subjected to 25 cycles of TVAC between −100 and +100 °C, with a heating rate of 5 °C min^{-1}.

As processing conditions are known to strongly affect the mechanical performance of LCPs,[30] four different printing temperatures T_{print} were tested, from 295 to 340 °C.

In Figure 7a, specimens tested in their axial direction show a decrease in Young's modulus with printing temperature. This trend is more apparent for pristine samples than TVAC samples. The span ranges from 35 GPa at T_{print} = 295 °C to 17 GPa at T_{print} = 340 °C for pristine samples, while it ranges from 25 to 15 GPa for the same printing temperatures, exposed to TVAC. UTS is also similarly affected by printing temperature. However here the same range (300 to 500 MPa) is covered by both pristine and TVAC samples. This decrease in performance with printing temperature is in line with previous findings and was attributed to the longer time available for the nematic domains to relax into a lesser-ordered state after extrusion, before reaching solidification temperature.[24]

For each printing temperature, thermal cycling appears to impact Young's modulus more than UTS. Even if UTS values are on average slightly smaller for TVAC samples than non-exposed, the scatter does not allow us to conclude on the impact of thermal cycling on strength, except at T_{print} = 310 °C where the discrepancy is significantly larger (503 ± 51 MPa vs 312 ± 49 MPa). In

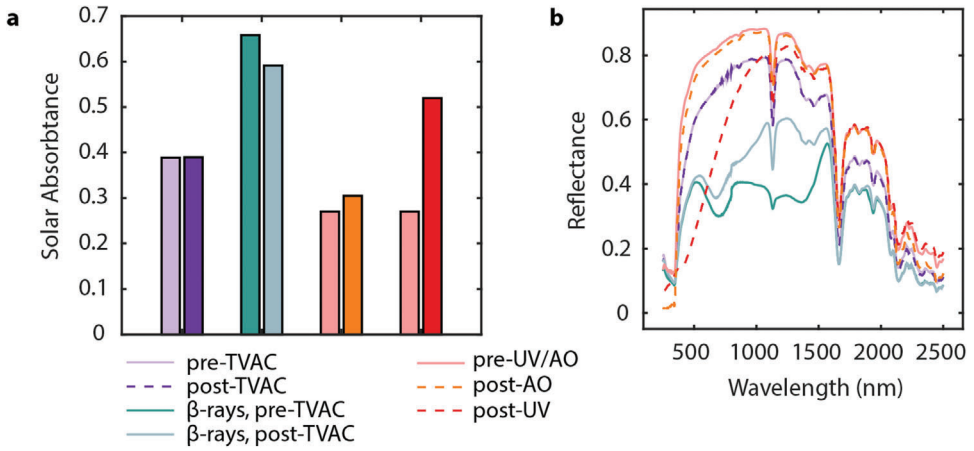

Figure 8. Change of optical properties of 3DP-LCP with different exposure types. A) Solar absorptance before and after exposure indicates that UVs have the largest impact among all exposure types due to its darkening effect. B) The reflectance spectrum of selected samples also indicates that a significant difference can be observed for samples exposed to β-rays.

contrast, the impact of TVAC on Young's modulus of samples is statistically significant at low printing temperatures. One should however take this result with caution, as these data were issued from two different batches. Even if care was spent on using the same g-code, same filament spool, and same printer, experience indicates that the parts produced at lower printing temperatures tend to also inevitably display higher variability in appearance and susceptibility to printing environment from one batch to another. At higher printing temperatures, in a similar manner to the UTS, a discrepancy between non-exposed and exposed samples is still present on average but becomes less statistically significant.

While loading in the X-direction seems to show a larger performance drop on Young's modulus than on UTS with increasing printing temperatures, this behavior changes when loading in the Z-direction. Figure 7b indicates that Young's modulus is not affected by printing temperature while strength improves with printing temperature, both for exposed and non-exposed samples. The improvement in strength, both for TVAC samples (from 2.9 ± 0.8 MPa to 6.6 ± 0.9 MPa) and for non-exposed samples (from 3.9 ± 0.4 MPa to 5.0 ± 0.3 MPa), is expected from past experiments with unidirectional samples tested 90° from their printing direction, still in the printing plane.[24,25] This series of experiments, normal to the printing plane, confirms the trend. While printing at low temperatures is beneficial to axial properties as shown in Figure 7a, it is detrimental to bonding strength. As a result, printing temperature may be leveraged for a trade-off between strength in the axial and transverse direction at different locations in the objects.

Results shown in Figure 7 indicate that there may be a drop in performance when exposing samples to TVAC, which seems more important at lower printing temperatures for the longitudinally-loaded specimen. This trend seems to decrease and even reverse for the transversally loaded samples with higher temperatures, for which TVAC appears to improve bonding.

These results also indicate that the variability of processing conditions plays a key role. The UTS of LCP is ≈400 MPa for the XY loading direction (in-plane, along the printed line direction) compared to ≈4 MPa in the XZ direction (normal to the printing plane). In comparison, these values are 95 to 13.4 MPa for PEEK[80] and 74 to 32 MPa for PEI[12] due to its amorphous nature. The highly anisotropic nature of 3DP-LCPs inevitably implies that the polymer chains, which are stiff and rigid in one direction, cannot engage with other layers in the same manner as flexible-chain polymers and result in the same level of adhesion.[81] This calls for the design of 3D-printed objects where loading perpendicular to the printing plane should be avoided, in a similar fashion to the adaptive growth of wood.[82]

2.3. Comparison of Optical Properties

Among all samples printed and exposed, not all samples could be mechanically tested due to restrictions in sample size, and availability of the exposure facility. However, all exposed specimens could be tested for space-relevant optical properties, namely solar absorptance in **Figure** 8a and UV/Vis/Near-Infrared reflectance spectra in Figure 8b before and after exposure. Solar absorptance represents the fraction of incident solar radiation that is absorbed by the material. Tracking its evolution with exposure is valuable, as the absorbed solar radiation is often the predominant external heat input to the spacecraft.[34]

Reference spectra are taken for each sample type before exposure. Indeed, the AO and UV-exposed samples are printed with a 0.05 mm layer height, while all other samples are printed at 0.1 mm layer height. Therefore their reflectance spectra even before exposure differ. As can be expected from Figure 5, the most significant difference in optical properties occurs with the high-dose irradiated specimen, shown with the full green line in Figure 8b. After TVAC, while no significant changes have been visually observed (in contrast to Figure 5d where color centers visibly disappear after just 1 h of exposure at 200 °C), the full spectrum reveals a partial degree of recovery toward the pre-TVAC reference represented by the lilac-dashed line, in the near-Infrared. Overall, the beige color of 3DP-LCP before exposure grants the specimens a relatively low value of solar absorptance. The impact of UV is however considerable by this metric, due to darkening shown in Figure 4a. This change of color and the resulting increasing absorptance should be carefully assessed depending on

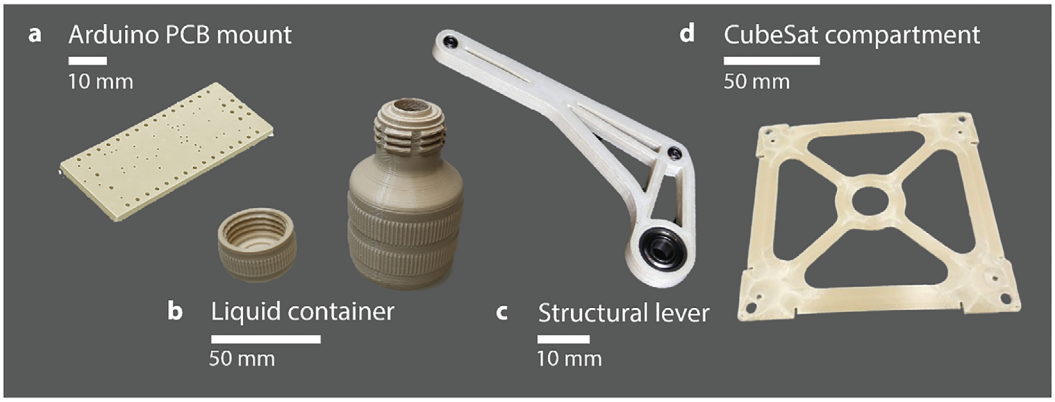

Figure 9. Possible use cases of 3D-printed LCP in space, with different scales of application manufactured with different 3D printers: A) an Arduino PCB mount, B) a screw-cap liquid container, C) a structural lever with bearings, and D) a compartment panel for a CubeSat.

the mission scenario. The ratio between absorptance and emissivity controls the temperature of the part's surface. An increasing ratio over time results in exposed surfaces becoming warmer than expected. If the material is directly exposed to the space radiative environment, a common practice is to apply protective coatings with long-lasting flight heritage to maintain such properties in time when thermo-optical performance is a key driver for spacecraft operability. Several potential applications of 3DP-LCP are shown in **Figure 9**. A PCB mount which requires high precision and modularity, and can also be thinned for wearable electronics, is printed with a micron-resolution 3D-printer NEX01 (NematX AG). The MELT zero gravity 3D printer from ESA was used to fabricate a screw-cap liquid container. A structural lever is also printed by an Ultimaker 2+, with inserted bearings, for use in a larger assembly. Finally, a CubeSat bus was printed with a Prusa MK3S+ 3D-printer. The diversity of printers used, and geometries possible demonstrates the overall versatility of 3D-printed LCPs in sustainable, structural, use cases.

3. Conclusion

The space-worthiness of 3D-printed LCP was evaluated. Specimens were exposed to four different simulated space environments: AO, Vacuum UV, electron irradiation, and thermal cycling. Surface damage caused by AO has been quantified and results in surface erosion comparable to other high-performance polymers such as PEEK and PEI. The effect of 6.7 solar constant worth of Vacuum UV is significant, indicating that like many other polymeric surfaces, its exposed use in space requires protection coatings to prevent surface damage, discoloration, and chain scission. Furthermore, bulk damage was targeted by choosing 1 MeV electrons, with three different doses. This has led to the observation of annealable color centers, for the first time, with 3D-printed polymers or liquid crystal polymers. The consequent coloring of the polymers with a green hue was recoverable after 1 h of exposure to 200 °C. The large change in optical appearance coincides with the increase in amplitude of peaks corresponding to C-H stretching in FTIR. This indicates a degree of structural change to the polymeric backbone. DMA also indicates a slight decrease in storage modulus with increasing fluence across the temperature range studied, which is in line with the hypothesis of chain scission. Nevertheless, the quasi-static tensile mechanical properties do not vary significantly with increasing dose.

The influence of thermal cycling across four different printing temperatures and two build orientations was also studied. Thermal cycling may cause a decrease in mechanical performance, especially at lower printing temperatures. This effect attenuates with increased printing temperature, as does the scatter in values. This can be explained by a higher sensitivity to small manufacturing errors and environmental fluctuations when the printing temperature is closer to the polymer solidification threshold. This result also illustrates the high anisotropy of LCP, with a 100-fold difference in strength between loading conditions longitudinal and normal to the printing planes, as opposed to a sevenfold or twofold difference for PEEK and PEI, respectively. Samples that are exposed to the maximum dose, 292 Mrad and then thermally-cycled under vacuum between −100 and +100 °C still display an average Young's modulus of 30 GPa and 503 MPa of UTS. The maximum ultimate tensile strength of 503 MPa of LCP is also more than five times larger than PEI.

We have concluded that akin to its melt-spun version which is already used in space, 3D-printed LCP remains a suitable material to consider for in-orbit applications or out-of-Earth manufacturing, and a great alternative to engineering polymers like PEEK or PEI. In an out-of-Earth mission scenario, several features of an anisotropic and recyclable material like LCP become useful throughout the life of a part: during the design phase, its anisotropy can help minimize material use by using concurrent topology and anisotropy optimization.[83,84] During manufacturing, its relative ease of printing with a desktop printer compared to approaches needing an enclosure and drastic thermal control such as PEEK or PEI can be associated with low energy consumption. During its use, its high mechanical performance and resistance to space exposure can maximize its service duration. Finally, the lack of additives or other materials such as fibers or compounds, facilitates its recyclability after end-of-life.[24]

4. Experimental Section

Specimen preparation—Feedstock Material: The 3D-printing filament of LCP is supplied by NematX AG (Switzerland) with a diameter of 1.75 mm. This filament is made of Vectra A950, the trademark for the

thermotropic random copolymer HBA:HNA with a ratio 73:27 (Celanese, USA).

3D Printer: Two 3D-printers were used for this study: a Ultimaker 2+ (Ultimaker, The Netherlands) which was modified with a direct-drive Hemera (E3D, England) printhead and a PT100 temperature sensor. A Prusa MK3S+ printer (Prusa, Czech Republic) was also modified to print up to 340 °C by changing the factory printhead to higher-temperature polycarbonate parts, adding a PT100 temperature sensor, and altering the firmware correspondingly. Figure 9 also contains a PCB mount produced with a NEX01 high-accuracy 3D-printer (NematX AG, Switzerland) and a liquid container produced by the MELT zero-gravity 3D-printer (ESA).

Specimen Geometry and Printing Parameters: Constant printing parameters in this study are bed temperature of 90 °C, 35 mm s^{-1} deposition speed, 0.35 mm line width, and 0% printing fan speed. The slicing was performed in Cura (Ultimaker, The Netherlands). The printing bed was coated with an adhesive (Dimafix, Spain) to maintain good adhesion. A brass nozzle with a diameter of 0.4 mm (E3D, England), was also used.

Specimen that were prepared for outgassing, AO and for UV exposure in Figures 2–4 were printed at a temperature of 295 °C on the Ultimaker 2+, with a layer height of 50 µm.

The sample geometries (25.4 × 25.4 × 2 mm rectangle for outgassing and UV, and cylinder of 20 mm diameter and 2 mm thickness for AO, corresponding to available sample holders) were printed with a rectilinear 100% infill, stacking sequence of [±45°], 3 perimeter walls and a printing temperature of 295 °C.

All the specimen prepared for mechanical testing in Figures 5–7 were printed on the Prusa MK3S+ printer at a printing temperature of 295 °C unless otherwise stated, with a layer height of 100 µm.

For in-plane testing in Figures 6a and 7a (printing direction aligned with loading direction), specimen dimensions of 5 × 2 × 110 mm were used. Slicing parameters chosen were 100% rectilinear (unidirectional) infill without perimeter. GFRP tabs were used to ensure a gauge length of 65 mm. These tabs were beveled at 45° to introduce the load gradually to the test section according to ISO 527-5.[85] The LCP specimen were sanded and cleaned at the tabbing zone, and then glued to the GFRP tabs with a strong adhesive (DP460, 3 M). A minimum of five specimen were printed per batch.

The dogbone sample, illustrated in Figure 7b, is 20 mm wide, and 65 mm tall, with a constant gauge length of dimensions LxWxD = 20 × 10 × 4 mm according to ISO 527-2.[86] A concentric 100% infill was used to print the specimen. Specimen were also sanded lightly on both faces before applying the speckle pattern for DIC in order to smoothen the layered effect caused by the additive manufacturing process, and reduce potential stress concentrations. Four specimen were printed per batch.

Exposure to Space Environment—Outgassing: Outgassing was performed with the µVCM vacuum chamber in ESTEC according to ECSS-Q-ST-70-02C.[87] Samples were conditioned for 24 h at 22 ± 3 °C and 55 ± 10% RH. During the test for 24 h, the sample was subjected to a temperature of 125 °C. The condensable material was collected by a collector plate, kept at 25 °C, while the test vacuum pressure was kept below 10^{-5} mbar. Post-test conditioning of the sample was 24 h at 22 ± 3 °C and 55 ± 10% RH.

A bake-out step was performed before the Residual Gas Analysis (RGA) study at 150 °C for 24 h. The RGA was performed both for baked-out and pristine samples.

Atomic Oxygen: Atomic Oxygen exposure was performed in the LEOX facility of ESTEC[88] where a pulsed CO_2 laser dissociates molecular O_2. The location of the sample holder led to a flux of 6.96×10^{15} atoms cm^{-2} s^{-1}, with a typical atomic oxygen energy of 5.5 eV. The mass of the sample before (M_{BOT}) and after the test (M_{EOT}) was measured to calculate the erosion yield E via the relationship $E = \frac{M_{BOT} - M_{EOT}}{A_s \rho_s F}$, where A_s is the exposure area, ρ_s is the sample density and F is the total atomic oxygen fluence, equal to 1.98×10^{21} atoms cm^{-2} in this experiment.

UV-Irradiation: Vacuum-UV irradiation was carried out in the Cross I facility of ESTEC.[89] The UV housing consists of high-pressure discharge UV lamps with an air fan and process water cooling. The UV source produces UV, visible, and IR radiation. The lamp unit was positioned outside the vacuum chamber. The radiation down to 200 nm was transmitted to the sample plate through the fused silica window. The lamps are powered by stabilized power supplies, which can be operated at a variable wattage from 270 to 600 W. The sample plate was radiated under an angle of ≈45°. UV intensity was measured with a calibrated UV detector, inside the facility before and after the test. It was then compared to the solar spectrum and averaged to obtain an acceleration factor, expressed in solar constants. The value of 6.7 solar constant was obtained.

Sample temperature was maintained between 65 and 100 °C. The pressure was kept below 1×10^{-5} mbar for a total test duration of 432 h, amounting to 2900 equivalent sun hours.

Beta Irradiation: A Van der Graaf accelerator (Radiation Institute, TU Delft) was used to accelerate electrons at 1 MV with a beam current varying between 64.4 and 67.5 µA, During irradiation, the table temperature was monitored and did not exceed 22 °C. The specimens were flushed with nitrogen throughout the exposure time, varying from 3 min to 5 h. Currents used, exposure time and dose rates obtained are specified in Table S1 (Supporting Information).

Thermal Cycling: Thermal vacuum cycling was performed in a specific chamber for 25 cycles from −100 to +100 °C with a vacuum level between 10^{-6} and 10^{-7} mbar using a 5 K min^{-1} heating rate and 30 min dwell time according to ECSS-Q-ST-70-04C.[90]

Post-Exposure Characterization—FTIR: FTIR was performed with a Spectrum 100 FTIR Spectrophotometer (PerkinElmer, USA), equipped with a universal ATR sampling accessory and Diamond/ZnSe crystal. Spectra were collected over a wavenumber range from 4000 to 600 cm^{-1}, with 2 cm^{-1} resolution, and were signal-averaged over 8 scans.

Mechanical Testing: Quasi-static tests were performed for two kinds of unidirectional samples in tension using an universal testing machine (Zwick-Roell, Germany).

The 0° samples in Figures 6a and 7a were clamped with hydraulic grips to avoid slippage of the samples from the tabs. Specimen were loaded at a strain rate of 2 mm min^{-1} and force was measured by a 10 kN Zwick load-cell. Fracture occurred by catastrophic splitting as shown in Figure S5 (Supporting Information).

For the dogbone specimen in Figure 7, rubber grips were used to load the specimen at a strain-rate of 0.5 mm min^{-1}. Force was recorded with a 1 kN load cell. No necking was observed before failure, which happened within the gauge length, in the interface between layers.

For the two specimen types, DIC was used to measure strain. Two 9 MP cameras were used (LIMESS, Germany) with a 50-mm focal length lense to acquire images at a rate of 2 Hz. Extraction of strain values was performed with the Vic 3D-8 (Correlated Solutions, USA) software.

Dynamical Mechanical Analysis was performed with a RSA G2 DMA bench (TA Instruments, USA) equipped with a furnace. Samples of size 25 × 5 × 2 were tested under three-point bending at a frequency of 10 Hz between 22 and 200 °C, with a span-length of 25 mm.

CTE Measurements: CTE values for different printing directions of 3DP LCP were extrapolated from TMA measurements, using a TMA Q400 (TA Instruments). Samples were 3D printed with a size of 50 × 50 × 5 mm, then cut into TMA specimens of 5 × 5 × 5 mm with a diamond saw. Specimens were heated up from 40 to 240 °C, with a heat rate of 2 °C min^{-1}. Each specimen underwent 3 heating cycles, and the average of the CTEs given at each round was taken.

Optical Measurements: A Cary 5000A UV/VIS/NIR spectrophotometer (Agilent, USA) fitted with an internal integrating sphere was used to acquire the total reflectance of the samples between 2500 and 250 nm under ambient conditions. Reflectance measurements were corrected against a calibrated Spectralon diffuse standard. For the determination of the Solar absorptance (α), total reflectance spectra were weighted against the Sun spectrum according to ESA ECSS-Q-70-09C and ASTM E490. The uncertainty of the solar absorptance determination through this method is ± 0.03 (confidence factor = 2).

Thermal emittance (ε) was measured using a TESA 2000B portable reflectometer/emissometer (AZ Technology, USA). The IR emittance was obtained by integrating over the spectral range from 3 to 30 µm and weighting it with the spectrum of a 300 K blackbody. The uncertainty for the IR

emittance measured with the portable equipment is ± 0.05 (confidence factor = 2).

Supporting Information

Supporting Information is available from the Wiley Online Library or from the author.

Acknowledgements

K.M. and C.H. acknowledge the support of ESA co-sponsored Research grant No. 4000131850. The authors also acknowledge the support of ESA for access to the Euro Material Ageing facility, in which 3DP-LCP samples will be integrated. The facility will be attached to the Bartolomeo platform,[91] ram-side of the International Space Station, in late 2024.

Conflict of Interest

S.G. and K.M. are co-inventors of a patent application on liquid crystal polymer 3D printing and co-founders of NematX AG.

Author Contributions

The conceptualization of this work was performed by C.H., K.M., S.G., T.R., U.L. Investigation was carried out by C.H., E.C., C.M., H.J., A.B., S.S., A.S. and U.L. The original draft was written by C.H. and K.M. All authors contributed to reviewing and editing. The project was supervised by K.M., U.L. and T.R. Administrative and funding acquisition efforts were carried out by S.V.B., H.J., R.H., U.L., T.R., and K.M.

Data Availability Statement

The data that support the findings of this study are available from the corresponding author upon reasonable request.

Keywords

3D-printing, anisotropy, bio-inspired materials, color centers, fused filament fabrication, liquid crystal polymers, space structures

Received: April 11, 2024
Revised: September 5, 2024
Published online:

[1] "Help ESA pave the way for a space circular economy", https://www.esa.int/Enabling_Support/Preparing_for_the_Future/Discovery_and_Preparation/Help_ESA_pave_the_way_for_a_space_circular_economy **2024**.
[2] G. Denis, D. Alary, X. Pasco, N. Pisot, D. Texier, S. Toulza, *Acta Astronaut.* **2020**, *166*, 431.
[3] E. Kulu, in 36th Annu. Small Satell. Conf **2022**.
[4] S. El-Shawa, B. Cattani, L. Innocenti, J. Delaval, in 72nd Int. Astronaut. Congr, IAF, Dubai, UAE **2021**, 1.
[5] A. Makaya, L. Pambaguian, T. Ghidini, T. Rohr, U. Lafont, A. Meurisse, *CEAS Sp. J.* **2023**, *15*, 69.
[6] A. Daurskikh, A. Sgambati, D. Graça, M. Berg, A. Baptista, M. Angelo, U. Lafont, in *Proc. 69th Int Astronaut. Congr*, Curran Associates, Inc., Bremen, Germany **2018**, pp. 1–5.
[7] K. Sertoglu, "ESA consortium develops high-temperature FFF 3D printer for the ISS", https://3dprintingindustry.com/news/esa-consortium-develops-high-temperature-fff-3d-printer-for-the-iss-187388/ **2021**.
[8] M. Ortega Varela de Seijas, M. Piskacev, L. Celotti, R. Nadalini, A. Daurskikh, A. Baptista, M. Berg, F. Caltavituro, I. Major, D. M. Devine, A. Maloney, U. Lafont, A. Makaya, *Acta Astronaut.* **2024**, *219*, 164.
[9] E. A. Slejko, A. Gregorio, V. Lughi, *Adv. Sp. Res.* **2021**, *67*, 1468.
[10] J. Gonçalves, P. Lima, B. Krause, P. Pötschke, U. Lafont, J. R. Gomes, C. S. Abreu, M. C. Paiva, J. A. Covas, *Polymers (Basel)* **2018**, *10*, 925.
[11] U. Lafont, B. Delacourt, M. Terol-Sanchez, M. Munck, J. Wessing, R. Rampini, in 9th Eur. Conf. Aeronaut. Space Sci., EUCASS, Lille, France **2022**.
[12] Y. Zhang, L. Yuan, C. Luo, X. Ren, Q. Gao, J. Chen, Q. Yu, Y. Cheng, A. Sun, G. Xu, J. Guo, *Eng. Fract. Mech.* **2024**, *297*, 109885.
[13] M. Yilmaz, N. F. Yilmaz, M. F. Kalkan, *J. Mater. Eng. Perform.* **2022**, *31*, 9900.
[14] B. Campbell, C. Nogales, B. Grim, M. Kamstra, J. Griffin, S. Parke, in Small Satell. Conf, Utah State University, Logan, USA **2020**.
[15] F. Sloan, *Structure Prop. High-Performance Fibers*, Elsevier Ltd, Amsterdam, Netherlands **2017**, pp. 113–140.
[16] G. Guerriero, R. Alderliesten, T. Dingemans, R. Benedictus, *Prog. Org. Coat.* **2011**, *70*, 245.
[17] K. F. Wissbrun, G. Kiss, F. N. Cogswell, *Chem. Eng. Commun.* **1987**, *53*, 149.
[18] D. Cadogan, C. Sandy, M. Grahne, *Acta Astronaut.* **2002**, *50*, 633.
[19] W. S. Kenner, T. C. Jones, V. M. Le Boffe, *Controlled Environmental Effects on Creep Test Data of Woven Fabric Webbings for Inflatable Space Modules (NASA/TM–2020-220561)*, NASA, Hampton USA, **2020**.
[20] "Sierra Space Sets the Stage for Pioneering Full-Scale 'Burst Test' of Expandable Space Station Module", https://www.sierraspace.com/newsroom/press-releases/sierra-space-sets-the-stage-for-pioneering-full-scale-burst-test-of-expandable-space-station-module/ **2023**.
[21] M. M. S. Mousavi, E. P. Ambrosio, S. Appendino, F. C. Chen, A. Favetto, D. Manfredi, F. Pescarmona, A. Somà, in 41st Int. Conf. Environ. Syst, ICES, Portland, USA **2011**, pp. 1–10.
[22] P. Weiss, M. P. Mohamed, T. Gobert, Y. Chouard, N. Singh, T. Chalal, S. Schmied, M. Schweins, T. Stegmaier, G. T. Gresser, G. Groemer, N. Sejkora, S. Das, R. Rampini, M. Hołyńska, *Adv. Sci. News* **2020**, *5*, 2000028.
[23] M. D. Fries, C. Lee, R. Bhartia, J. Razzell Hollis, L. W. Beegle, K. Uckert, T. G. Graff, W. Abbey, Z. Bailey, E. L. Berger, A. S. Burton, M. J. Callaway, E. L. Cardarelli, K. N. Davis, L. DeFlores, K. S. Edgett, A. C. Fox, D. H. Garrison, N. C. Haney, R. S. Harrington, R. S. Jakubek, M. R. Kennedy, K. Hickman-Lewis, F. M. McCubbin, E. Miller, B. Monacelli, R. Pollock, R. Rhodes, S. Siljeström, S. Sharma, et al., *Space Sci. Rev.* **2022**, *218*, 46.
[24] S. Gantenbein, K. Masania, W. Woigk, J. P. W. Sesseg, T. A. Tervoort, A. R. Studart, *Nature* **2018**, *561*, 226.
[25] S. Gantenbein, C. Mascolo, C. Houriet, R. Zboray, A. Neels, K. Masania, A. R. Studart, *Adv. Funct. Mater.* **2021**, *31*, 2104574.
[26] C. Houriet, V. Damodaran, C. Mascolo, S. Gantenbein, D. Peeters, K. Masania, *Adv. Mater.* **2023**, *36*, 2307444.
[27] B. Seshadri, I. Hischier, K. Masania, A. Schlueter, *Adv. Mater. Technol.* **2023**, *8*, 2300403.
[28] J. W. C. C. Dunlop, R. Weinkamer, P. Fratzl, *Mater. Today* **2011**, *14*, 70.
[29] A. Romo-Uribe, A. Reyes-Mayer, M. Calixto Rodriguez, E. Sarmiento-Bustos, *Polymer (Guildf)* **2022**, *240*, 124506.
[30] D. E. Turek, G. P. Simon, *Polymer (Guildf)* **1993**, *34*, 2763.
[31] G. Wiberg, H. Hillborg, U. W. Gedde, *Polym. Eng. Sci.* **1998**, *38*, 1278.
[32] J. Allum, A. Moetazedian, A. Gleadall, V. V. Silberschmidt, *Addit. Manuf.* **2021**, *48*, 102390.
[33] A. Das, E. L. Gilmer, S. Biria, M. J. Bortner, *Appl. Polym. Mater.* **2021**, *3*, 1218.

[34] K. K. De Groh, B. A. Banks, S. K. R. Miller, J. A. Dever, *Handbook of Environmental Degradation of Materials*, (Third Edition), William Andrew Publishing, Norwich, USA **2018**, pp. 601–645.
[35] A. Suliga, J. Wessing, A. Hand, A. Tighe, S. Vincent-Bonnieu, R. Rampini, in IOP Conf. Ser. Mater. Sci. Eng. **2023**, *1287*, 012026.
[36] A. Suliga, O. Ergincan, R. Rampini, *Syst. Contam. Predict. Control. Perform.* **2020**, *11489*, 50.
[37] J. Yang, K. de Groh, *MRS Bull.* **2010**, *35*, 12.
[38] "Outgassing Properties of Vectran – NASA Outgassing Data Base", https://data.nasa.gov/Applied-Science/Outgassing-Db/r588-f7pr/about_data, Goddard Space Flight Center, NASA, **2015**.
[39] ECSS-Q-ST-70-02C, *Thermal Vacuum Outgassing Test for the Screening of Space Materials*, ECSS, Noordwijk, Netherlands **2008**.
[40] C. R. Stidham, T. J. Stueber, B. A. Banks, J. A. Dever, S. K. Rutledge, in Int. SAMPE Sympos. Exhibit, May **1993**, 106128.
[41] G. Bitetti, S. Mileti, M. Marchetti, P. Miccichè, in Proc. of the 10th ISMSE & the 8th ICPMSE, Collioure, France, July **2006**, pp. 19–23.
[42] K. K. de Groh, B. A. Banks, *Atomic Oxygen Erosion Data From the MISSE 2–8 Missions*, NASA, OH, USA **2019**.
[43] G. T. Yi, K. K. De Groh, B. A. Banks, A. Haloua, E. C. Imka, G. G. Mitchell, in Int. Symp. Mater. Sp. Environ, Noordwijk, September **2013**.
[44] B. A. Banks, K. K. De Groh, S. K. Miller, *MRS Online Proc. Libr.* **2004**, *851*, 426.
[45] M. M. Finckenor, G. C. Marshall, *Comparison of High-Performance Fiber Materials Properties in Simulated and Actual Space Environments (NASA/TM—2017–219634)*, NASA, OH, USA **2017**.
[46] ANSYS. Inc., "Ansys Granta EduPack Database", http://www.ansys.com/materials **2021**.
[47] G. R. Cool, *Atomic Oxygen Erosion Resistance of Organic Polymers for Low Earth Orbit Spacecraft*, University of Toronto, Toronto Canada **1996**.
[48] M. M. Finckenor, J. A. Vaughn, E. Watts, in 42nd AIAA Aerosp. Sci. Meet. Exhib, AIAA, Reno, Nevada **2004**, 322.
[49] K. K. De Groh, B. A. Banks, O. C. Asmar, E. A. Sechkar, *Erosion Results of the MISSE 8 Polymers Experiment After 2 Years of Space Exposure on the International Space Station (NASA/TM—2017-219445)*, NASA, OH United States **2017**.
[50] J. A. Dever, *Low Earth Orbital Atomic Oxygen and Ultraviolet Radiation Effects on Polymers (NASA/TM-1991-103711)*, NASA, OH United States **1991**.
[51] Y. Liu, Y. Liu, H. Tan, C. Wang, H. Wei, Z. Guo, *Polym. Degrad. Stab.* **2013**, *98*, 1744.
[52] M. R. Adams, *The Degradation of Polymeric Spacecraft Materials by Far-UV Radiation and Atomic Oxygen*, University of Connecticut, MI USA **1993**.
[53] Y. Liu, Y. Liu, C. Zhang, H. Tan, X. Yan, H. Wei, Z. Guo, *Macromol. Mater. Eng.* **2015**, *300*, 64.
[54] J. He, Z. Liu, W. Zhang, C. He, W. Li, *Surfaces and Interfaces* **2023**, *42*, 103477.
[55] K. Dawes, L. C. Glover, D. A. Vroom, *Physysical. Properties Polymers. Handbook*, Springer, New York **2007**, pp. 867.
[56] G. Dietze, D. T. Bartlett, D. A. Cool, F. A. Cucinotta, X. Jia, I. R. McAulay, M. Pelliccioni, V. Petrov, G. Reitz, T. Sato, *Ann. ICRP* **2013**, *42*, 1.
[57] D. Matthiä, D. M. Hassler, W. de Wet, B. Ehresmann, A. Firan, J. Flores-McLaughlin, J. Guo, L. H. Heilbronn, K. Lee, H. Ratliff, R. R. Rios, T. C. Slaba, M. Smith, N. N. Stoffle, L. W. Townsend, T. Berger, G. Reitz, R. F. Wimmer-Schweingruber, C. Zeitlin, *Life Sci. Sp. Res.* **2017**, *14*, 18.
[58] M. Fruit, F. Berghmans, G. Ulbrich, A. Gussarov, D. Doyle, in Proc. – Int. Conf. Sp. Opt. **2017**, *10569*, 56.
[59] D. Nikezic, M. S. Beni, D. Krstic, K. N. Yu, *PLoS One* **2016**, *11*, 0157627.
[60] F. Seitz, *Rev. Mod. Phys.* **1946**, *18*, 384.
[61] R. L. Clough, K. T. Gillen, G. M. Malone, J. S. Wallace, *Radiat. Phys. Chem.* **1996**, *48*, 583.
[62] J. S. Wallace, M. B. Sinclair, K. T. Gillen, R. L. Clough, *Radiat. Phys. Chem.* **1993**, *41*, 85.
[63] J. P. Harmon, J. F. Gaynor, A. G. Taylor, *Radiat. Phys. Chem.* **1993**, *41*, 153.
[64] S. A. Nouh, R. A. Bahareth, *Radiat. Eff. Defects Solids* **2012**, *167*, 766.
[65] J. S. Peng, C. M. Hsu, S. H. Yeh, S. Lee, *Polym. Eng. Sci.* **2012**, *52*, 2391.
[66] C. K. Liu, C. J. Tsai, C. T. Hu, S. Lee, *Polymer (Guildf)* **2005**, *46*, 5645.
[67] M. I. Fulton, P. J. Pomery, N. A. St John, G. A. George, *Polym. Adv. Technol.* **1998**, *9*, 75.
[68] L. Hou, Y. Wu, J. Xiao, B. Guo, Y. Zong, *Nucl. Instruments Methods Phys. Res. Sect. B* **2019**, *439*, 1.
[69] G. Socrates, *Infrared and Raman Characteristic Group Frequencies: Tables and Charts*, John Wiley And Sons Inc, New York **2004**.
[70] J. G. Funk, G. F. Sykes, *Effects of Simulated Space Environmental Parameters on Six Commercially Available Composite Materials (NASA/TM-1989-2906)*, NASA, Hampton USA **1989**.
[71] D. J. Blundell, K. A. Buckingham, *Polymer (Guildf)* **1985**, *26*, 1623.
[72] M. J. Troughton, G. R. Davies, I. M. Ward, *Polymer (Guildf)* **1989**, *30*, 58.
[73] J.-P. Williams, D. A. Paige, B. T. Greenhagen, E. Sefton-Nash, *Icarus* **2017**, *283*, 300.
[74] A. Anvari, *J. Eng.* **2020**, *2020*, 1.
[75] R. B. Fette, M. F. Sovinski, *Vectran Fiber Time-Dependent Behavior and Additional Static Loading Properties (NASA/TM—2004-212773)*, NASA, MD United States **2004**.
[76] D. I. Green, G. A. J. Orchard, G. R. Davies, I. M. Ward, *J. Polym. Sci. Part B Polym. Phys.* **1990**, *28*, 2225.
[77] J. L. Colón Quintana, L. Slattery, J. Pinkham, J. Keaton, R. A. Lopez-Anido, K. Sharp, *Materials (Basel)* **2022**, *15*, 2764.
[78] J. B. Nelson, D. P. Riley, *Proc. Phys. Soc.* **1945**, *57*, 477.
[79] L. Zhao, J. Tang, M. Zhou, K. Shen, *New Carbon Mater* **2022**, *37*, 544.
[80] Q. Xu, W. Xu, Y. Yang, X. Yin, C. Zhou, J. Han, X. Li, Y. Shang, H. Zhang, *Addit. Manuf.* **2022**, *55*, 102852.
[81] T. J. Coogan, D. O. Kazmer, *Addit. Manuf.* **2020**, *35*, 101368.
[82] R. Weinkamer, P. Fratzl, *Mater. Sci. Eng. C* **2011**, *31*, 1164.
[83] M. P. Schmidt, L. Couret, C. Gout, C. B. W. Pedersen, *Struct. Multidiscip. Opt.* **2020**, *62*, 3105.
[84] R. D. Kundu, X. S. Zhang, *Addit. Manuf.* **2023**, *75*, 103730.
[85] Part 5: Test conditions for unidirectional fibre-reinforced plastic composites, International Organization of Standardization, **2009**.
[86] Part 2: Test conditions for moulding and extrusion plastics, International Organization of Standardization, **2012**.
[87] ECSS-Q-ST-70-02C, *Space Product Assurance, Thermal Vacuum Outgassing Test for the Screening of Space Materials*, ECSS, Noordwijk, Netherlands **2008**.
[88] A. Tighe, "Overview of the LEOX Test facility", https://esamultimedia.esa.int/multimedia/industry/ESA_TECQE_AO_013375.pdf, **2019**.
[89] S. Heltzel, C. Semprimoschnig, M. Moser, M. van Eesbeek, in Spacecr. Struct. Mater. Mech. Test, Noordwijk, Netherlands, May **2005**.
[90] ECSS-Q-ST-70-04C, *Thermal Testing for the Evaluation of Space Materials, Processes, Mechanical Parts and Assemblies*, ECSS, Noordwijk, Netherlands **2008**.
[91] B. Corley, P. C. Steimle, *AIAA Sci. Technol. Forum Expo. AIAA Sci. Tech. Forum*, AIAA, San Diego USA **2022**, *2022*, 1.